



# Deconvolution of acoustically detected bubble-collapse shock waves



Kristoffer Johansen<sup>a</sup>, Jae Hee Song<sup>a</sup>, Keith Johnston<sup>b</sup>, Paul Prentice<sup>a,\*</sup>

<sup>a</sup> Cavitation Laboratory, School of Engineering, University of Glasgow, Glasgow G12 8QQ, United Kingdom

<sup>b</sup> Division of Imaging and Technology, School of Medicine, University of Dundee, Dundee DD1 9SY, United Kingdom

## ARTICLE INFO

### Article history:

Received 2 May 2016

Received in revised form 6 September 2016

Accepted 7 September 2016

Available online 9 September 2016

### Keywords:

Bubble  
Collapse  
Shock wave  
Deconvolution

## ABSTRACT

The shock wave emitted by the collapse of a laser-induced bubble is detected at propagation distances of 30, 40 and 50 mm, using a PVdF needle hydrophone, with a non-flat end-of-cable frequency response, calibrated for magnitude and phase, from 125 kHz to 20 MHz. High-speed shadowgraphic imaging at  $5 \times 10^6$  frames per second, 10 ns temporal resolution and 256 frames per sequence, records the bubble deflation from maximum to minimum radius, the collapse and shock wave generation, and the subsequent rebound in unprecedented detail, for a single sequence of an individual bubble. The Gilmore equation for bubble oscillation is solved according to the resolved bubble collapse, and simulated shock wave profiles deduced from the acoustic emissions, for comparison to the hydrophone recordings. The effects of single-frequency calibration, magnitude-only and full waveform deconvolution of the experimental data are presented, in both time and frequency domains. Magnitude-only deconvolution increases the peak pressure amplitude of the measured shock wave by approximately 9%, from single-frequency calibration, with full waveform deconvolution increasing it by a further 3%. Full waveform deconvolution generates a shock wave profile that is in agreement with the simulated profile, filtered according to the calibration bandwidth. Implications for the detection and monitoring of acoustic cavitation, where the role of periodic bubble collapse shock waves has recently been realised, are discussed.

© 2016 Elsevier B.V. All rights reserved.

## 1. Introduction

The collapsing bubble plays a critical role in many inertial cavitation applications. The high energy densities that can be reached around the instant of collapse are known to mediate plasma [1] and free radical [2,3] formation, as well as picosecond pulses of light known as sonoluminescence [1,4]. In many reports, acoustic detection of the bubble collapse shock wave (BCSW) is undertaken with polyvinylidene fluoride (PVdF) needle-type hydrophone [5–11], and an apparent negative phase indicated within the profile [8–14], trailing the positive compressive pulse that characterise shock waves generally. The negative phase is not often discussed in any detail, but could be interpreted as the detection of a tensile pressure phase, generated via medium response to the propagation of a compressive pulse. Such ‘wake-effects’ are well documented for the shock waves generated during lithotripsy, for example, although diffraction at the lithotripter aperture also provides a contribution to the tensile phase [15].

The emission of single shock waves from a closely packed cloud of bubbles, generated by a short burst of intense focused

ultrasound incident to a surface, has also been observed via high-speed imaging and acoustically detected with a needle-type hydrophone [10]. In this work, the bubble cloud forms around the acoustic focus, with component bubbles expanding and collapsing in unison to produce a single shock front. Our group has also reported that the component bubbles within a cloud acoustically driven by an extended burst of focused ultrasound, oscillate in phase such that the cloud emits single shock waves – although multi-fronted shock waves were observed for larger clouds and higher driving pressure amplitudes – periodically, at subharmonic frequencies to that of the driving [16]. Although BCSWs are recognised as an acoustic signal generated by inertial cavitation activity, it is generally thought that shock waves primarily contribute to the cavitation spectrum by raising the power of all spectral features [17]. Periodic shock waves, however, can be responsible for specific features, particularly the subharmonic and higher-order subharmonic peaks. The treatment of the detected shock waves could have implications for the spectra presented in reports on acoustic cavitation effects.

In this paper we report on the use of a commercial PVdF needle hydrophone, supplied with a pre-amplifier, and end-of-cable calibration for both magnitude and phase over a bandwidth of 125 kHz to 20 MHz, to detect the BCSW emitted during the collapse

\* Corresponding author.

E-mail address: [paul.prentice@glasgow.ac.uk](mailto:paul.prentice@glasgow.ac.uk) (P. Prentice).

of a laser-induced bubble (LIB) in water. Consistent with previous reports [8–14], the raw hydrophone data indicate an apparent negative phase in the voltage output of the detected BCSW profile, at all propagation distances over which measurements are taken. We present BCSW measurements under the assumption of single-frequency calibration, magnitude-only deconvolution, and full waveform deconvolution with complex sensitivity over the calibrated bandwidth. It should be recognised that such a hydrophone device, which may be expected to have a non-flat frequency response, is therefore not ideal for making such a measurement of broadband signals [18]. The measurement will be distorted, both with regards to the temporal shape and the relative magnitudes of the different frequency components [19,20]. Indeed, detectors have been developed with a smooth and predictable frequency response, for which single-frequency calibration is sufficient [21]. Here, we demonstrate that the shock wave measurement can be reasonably reconstructed with full waveform deconvolution, correcting for distortions imposed by the hydrophone frequency response. We use a common bubble oscillation model to simulate the LIB collapse and BCSW generation, with particular attention given to the peak pressure amplitude (PPA), the full width half maximum (FWHM) and the apparent negative phase of the experimental BCSW profile.

## 2. Experimental setup

When a laser pulse of energy sufficient to cause optical breakdown, is focused into a liquid, a single laser-induced bubble (LIB) forms. A LIB initially undergoes an expansion phase in response to the energy deposition, which the inertia of the host medium decelerates eventually causing the bubble to contract and collapse, often followed by several rebound oscillations. Acoustic detection of the LIB process is characterised by the emission of a series of shock waves. The first is generated by the plasma formed on absorption of the laser pulse [5], with a second emitted during the collapse of the primary bubble after a duration equal to the oscillation period of the LIB. Successive rebounds may also emit shocks of diminishing pressure amplitudes.

To study the BCSWs reliably, LIBs are generated within a custom built chamber, represented schematically by Fig. 1(a) measuring  $420 \times 438 \times 220 \text{ mm}^3$  and filled with degassed, deionised water. Two of the walls are recessed, allowing imaging optics to be placed in proximity to the intended location of the LIB, facilitating spatial resolution at  $7.6 \pm 0.1 \mu\text{m}$  per pixel. A single  $4.0 \pm 0.2 \text{ mJ}$  (instrument error according to manufacturer), 6–8 ns laser pulse (Nano S 130-10 frequency doubled Q-switched Nd:YAG, Litron Lasers, UK), is brought to a focus through a long working distance microscope objective lens ( $50 \times 0.42 \text{ NA}$  Mitutoyo, Japan), submerged in a sealed unit, and mounted on an xyz manipulator (Velmex Motor, Bloomfield, NY, USA). High-speed shadowgraphic imaging of the resulting cavitation activity is undertaken at  $5 \times 10^6$  frames per second (HPV-X2, Shimadzu, Japan), with synchronous 10 ns laser pulses (CAVILUX Smart, Cavitator, Finland) providing the illumination and effective temporal resolution. A delay generator (DG535, Stanford Research Systems, USA) provides electronic triggering to synchronise each of the instruments.

The HPV-X2 camera offers 256 frames per image sequence, such that the dynamics of the collapse of a single bubble is sampled sufficiently for modelling purposes, as described in Section 3. Much of the literature on this type of experiment relies on the selection of frames from a number of different high-speed sequences of a number of different bubbles, under the assumption that each bubble reaches an equivalent maximum radius and undergoes an equivalent collapse [5,22].

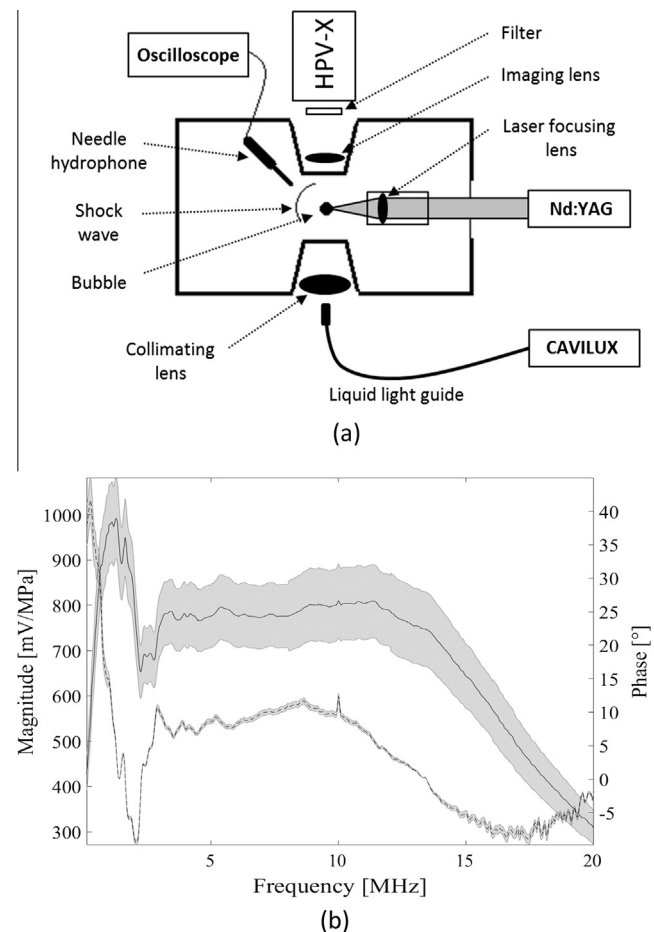
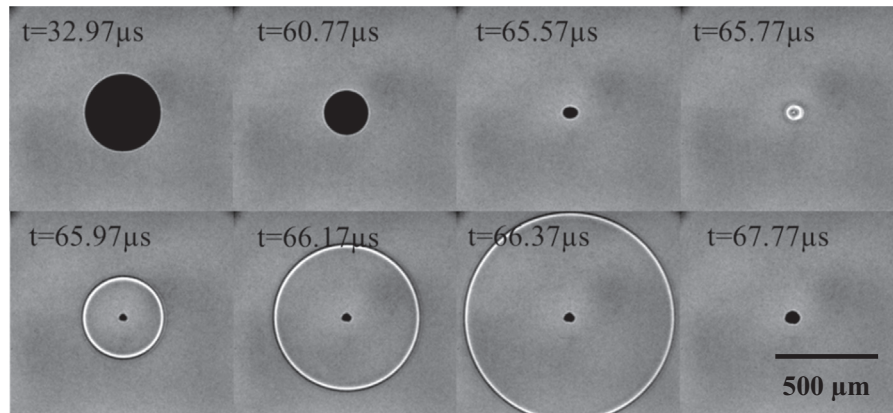


**Fig. 1.** (a) Schematic of the experimental configuration used for generating LIBs and detecting BCSWs with a 1 mm PVdF (Precision Acoustics) needle hydrophone. (b) End-of-cable magnitude (solid) and phase (dash) response for the needle hydrophone and pre-amplifier, over a bandwidth of 125 kHz–20 MHz in 25 kHz increments. Uncertainties are represented by the grey shading at 9–12% for the sensitivity and 4–8% for the phase, as provided by National Physical Laboratory (NPL).

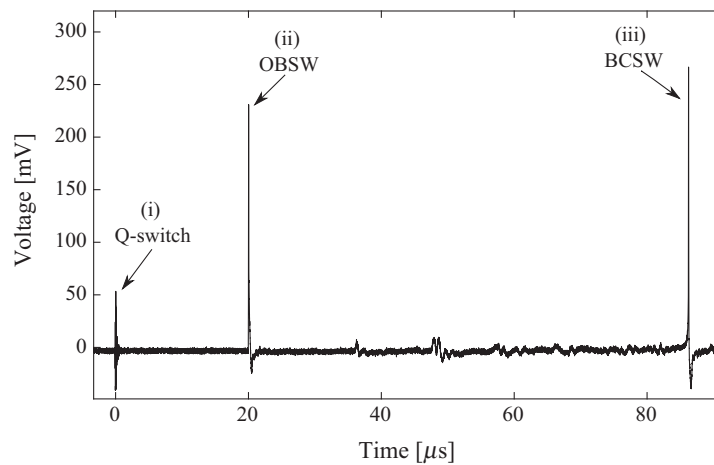
A PVdF needle hydrophone (1.0 mm diameter, 28  $\mu\text{m}$  thick active element, supplied with pre-amplifier, Precision Acoustics, UK), calibrated for both magnitude and phase over a bandwidth of 125 kHz–20 MHz, Fig. 1(b) (National Physical Laboratory (NPL), 2016), also mounted on an xyz manipulator, is positioned vertically over the bubble site to minimise reflections from the front face of the laser focusing lens unit. The fluctuations in both magnitude and phase illustrate the non-flat response of the hydrophone, and the need for detector deconvolution when measuring a broadband signal. The manufacturer of the needle hydrophone used in this study defines the frequency response to be flat when the variation is less than  $\pm 2 \text{ dB}$ . As such, the hydrophone response in the frequency range 4–12 MHz, may be considered flat, with the fluctuations occurring at  $< 4 \text{ MHz}$  and  $> 12 \text{ MHz}$ , Fig. 1(b).

Acoustic BCSW measurements are undertaken at distances of 30, 40 and 50 ( $\pm 0.5$ ) mm. At these distances the angle subtended by the 1 mm active area of the needle hydrophone is  $< 1^\circ$ , and the shock wave may be assumed planar to a first approximation. At shorter distances, the curvature of the shock wave would have a pronounced effect on the measured characteristics, including the FWHM, through geometric spreading across the active area. The hydrophone is connected to an oscilloscope (MS07104A, Agilent Technologies, USA), and acoustic data collected at  $4 \text{ GS}^{-1}$ .

Fig. 2(a) are representative frames extracted from a single high-speed image sequence, captured at  $5 \times 10^6$  frames per second, but with each frame exposed for only 10 ns. The criteria for an LIB



(a)



(b)

**Fig. 2.** (a) Representative high-speed images of an LIB collapse, BCSW generation and rebound, recorded at  $5 \times 10^6$  frames per second. Full image sequence available in movie format, as supplementary material. (b) A full hydrophone voltage trace, recorded at 30 mm, with key features described in the text, arrowed. Note, there is  $\sim 20 \mu\text{s}$  propagation time for the shock waves between the high-speed imaging capture and hydrophone detection.

collapse and BCSW to be included in the dataset from which profiles are considered, are (i) an  $R_{max} = 365 \pm 4 \mu\text{m}$ , Fig. 2(a) at 32.97  $\mu\text{s}$ , (ii) single fronted BCSW generation, Fig. 2(a) from 65.97 to 66.37  $\mu\text{s}$ , and (iii) a spherical post-collapse rebound, Fig. 2(a) at 67.77  $\mu\text{s}$ . It is well known that the size of a bubble is critical in determining the amplitude of the BCSW generated when it collapses [10]. To make meaningful comparisons between BCSW profiles at different propagation distance, equivalent  $R_{max}$ 's are critical, (i). It is also well reported that due to spherical aberration, there is an extended focal region for a laser pulse passed through an objective lens. The plasma generated, and the LIB that forms, will therefore be slightly elliptical [22], which is seen at 65.57  $\mu\text{s}$ , Fig. 2(a). A common observation made during the collection of this data was that in the event that the plasma generated on laser pulse absorption is too extended, the collapse could occur at two separate locations, generating a double-fronted shock wave. Moreover for such cases, the rebounded bubble will have fragmented, and such data was not considered further.

Fig. 2(b) is the voltage trace recorded by the needle hydrophone during the LIB collapse of Fig. 2(a). Notable features are arrowed, including (i) the Q-switch of the laser, indicating laser-pulse emission, which is taken as  $t = 0 \mu\text{s}$  for all data presented, (ii) the optical breakdown shock wave (OBSW), indicating laser absorption and plasma formation, and (iii) the BCSW, detection of which is the topic of this work.

An important characteristic of any hydrophone used to measure a shock wave is the rise time (RT) of the instrument, which is the

time taken to rise from 10 to 90% of the maximum voltage signal amplitude, in response to a unit step function. The OBSW has an abrupt rise to maximum signal [5], within a few ns – in contrast to that of the BCSW, which has a much smoother transition to PPA, due to the bubble emissions as it deflates into the collapse, Fig. 2(b) – which can be used to approximate an impulse response. Accordingly, an upper bound of 22.5 ns was deduced as the RT for the needle hydrophone used in this work. This suggests that the needle hydrophone has actual bandwidth beyond the 125 kHz–20 MHz calibration limit. All measured shock wave FWHMs stated in the results below are greater than this upper bound, and can therefore be taken as representative [5].

### 3. Bubble oscillation and shock wave generation model

There are many Rayleigh-Plesset-like equations in the literature that account for liquid compressibility [22–27]. These equations become relevant when the Mach number  $\frac{\dot{R}}{c_0}$  becomes 'small' during expansion [28], where  $c_0$  is the speed of sound far from the bubble, and  $\dot{R}$  is the bubble wall velocity. Examples of first order formulations are the Keller-Miksis [23] and Herring-Trilling [24] equations, whereas the Gilmore equation contains additional second order terms [25]. As the Gilmore equation depends on the liquid enthalpy,  $H$ , at the bubble wall, it is well suited to study inertial collapses [28]. Hence, the Gilmore equation is used in this work.

The formulation presented is taken from Kreider et al. with some modifications [26].

The Gilmore equation can be represented the following way

$$\left(1 - \frac{\dot{R}}{C}\right) R \ddot{R} + \frac{3}{2} \left(1 - \frac{\dot{R}}{3C}\right) \dot{R}^2 = \left(1 + \frac{\dot{R}}{C}\right) H + \left(1 - \frac{\dot{R}}{C}\right) \frac{R}{C} \dot{H}, \quad (1)$$

where the overdot represents the time derivative,  $R$  is the instantaneous radius, and  $C$  the instantaneous speed of sound evaluated at the bubble wall, respectively. Using a modified form of the Tait equation for the liquid state to express  $C$  and  $H$  explicitly [29].

$$p = p_0 + \frac{1}{b\Gamma} \left[ \left(\frac{\rho}{\rho_0}\right)^\Gamma - 1 \right] \quad (2)$$

where  $p_0$  is the ambient pressure,  $b$  and  $\Gamma$  are empirically determined constants,  $\rho$  and  $\rho_0$  are the instantaneous and ambient densities of the liquid, respectively.  $\Gamma = 6.5$  was chosen from data for water [29], and  $b$  is defined the following way  $b = (\rho_0 c_0^2)^{-1}$ .

The enthalpy  $H$  and the speed of sound  $C$  at the bubble wall is expressed as:

$$H = \frac{(b\Gamma)^{\frac{1}{\Gamma-1}}}{\rho_0} \frac{\Gamma}{\Gamma-1} \left[ (p_w - B)^{\frac{\Gamma-1}{\Gamma}} - (p_0 + B)^{\frac{\Gamma-1}{\Gamma}} \right], \quad (3)$$

and

$$C^2 = c_0^2 + (\Gamma - 1)H, \quad (4)$$

where  $B \equiv ((b\Gamma - p_0))^{-1}$  and  $p_w$  is the pressure at the bubble wall, where  $p_w$  can be expressed as

$$p_w = p_i - \frac{4\mu\dot{R}}{R} - \frac{2\sigma}{R}, \quad (5)$$

where  $p_i$  is the internal pressure in the bubble,  $\mu$  is the shear viscosity of the surrounding liquid and  $\sigma$  the surface tension at the gas-liquid interface. Assuming that the internal pressure is uniform, it can be represented as

$$p_i = \left( p_0 + \frac{2\sigma}{R_0} \right) \left( \frac{R_0^3 - mR_0^3}{R^3 - mR_0^3} \right)^\kappa, \quad (6)$$

where  $R_0$  is the equilibrium radius of the bubble, and  $m$  is the van der Waals core parameter, chosen as  $m = 0.11$ ,  $\kappa$  is the polytropic exponent. Now, the speed of sound and the enthalpy at the bubble wall can be explicitly expressed for implementation in a numerical scheme.

The formulation of Eq. (1) assumes a constant gas content of the bubble with a uniform pressure inside.

This has been shown to be an adequate assumption, even for inertial collapses [30]. A recent finite volume investigation of the collapse of a laser bubble, demonstrated that there are differences in both the internal pressure of the bubble, and the maximum rebound radius, compared to that predicted by the Gilmore equation [31]. Evaporation, condensation, gas diffusion through the bubble wall, and heat conduction are neglected.

The circle scatter plot of Fig. 3 is the radius measured from each frame of the high-speed sequence of the single LIB collapse, represented in Fig. 2(a). Other LIB radius-time curves reported have been at higher frame rates, but the authors rely on compiling the curve from multiple sequences of different LIBs, assuming identical bubble behaviour [5,22]. We also assign an error to the radius of the bubble, depicted as the shaded region of the circle scatter plot, based on bubble boundary pixel ambiguity within each image. We further note that the minimum pixel radius value, at 65.77  $\mu\text{s}$  for the LIB of Fig. 2(a), is likely underestimated as the BCSW generation and initial propagation obscures the bubble image.

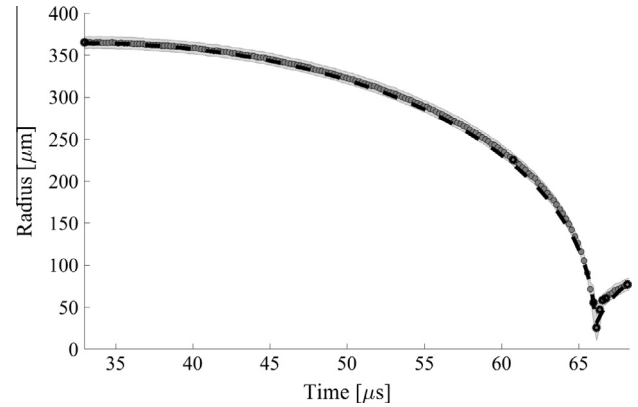
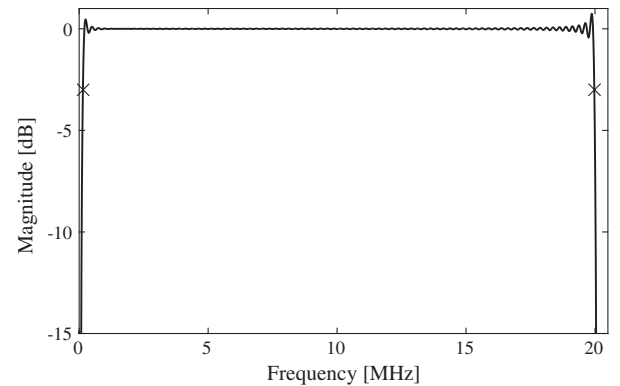


**Fig. 3.** The experimental radius-time curve (circles), of the bubble collapse depicted in Fig. 2(a) (bold circles are the data points of the images presented). The dashed line curve is the best fit solution of the Gilmore equation with the following parameters, for water;  $c_0 = 1484 \text{ m s}^{-1}$ ,  $p_0 = 101 \text{ kPa}$ ,  $R_0 = 61 \text{ }\mu\text{m}$ ,  $R_{\text{max}} = 364 \text{ }\mu\text{m}$ ,  $\rho_0 = 998 \text{ kg m}^{-3}$ ,  $\sigma = 0.072 \text{ N m}^{-1}$  and  $\mu = 0.001 \text{ Pa s}$ .

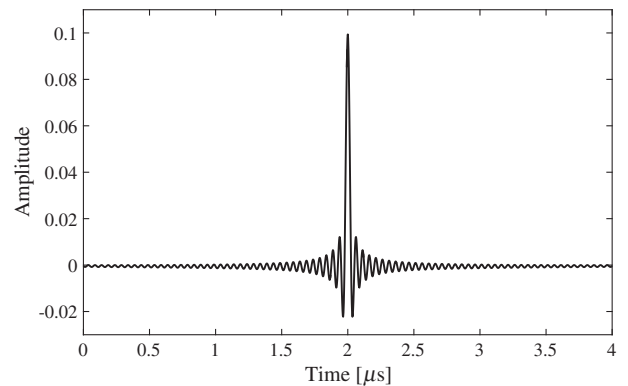
Solving Eq. (1) for the bubble deflation, collapse and rebound, dashed curve of Fig. 3, allows the dynamics around the simulated collapse to be probed in more detail. The acoustic emission as a spherical wave,  $P_{\text{rad}}$ , can be calculated the following way [13]:

$$P_{\text{rad}} = \rho_0 \frac{R^2 \ddot{R} + 2R\dot{R}^2}{r}, \quad (7)$$

where  $r$  is distance from the centre of the cavity. This approach is used to generate the simulated shock wave profiles, presented in dashed line, Figs. 5–7. Simulated shock wave profiles at all propagation distances are computed with a bandwidth of 100 MHz.



(a)



(b)

**Fig. 4.** (a) Magnitude response of zero-phase bandpass filter,  $H_{\text{bpf}}(f)$ , with the  $-3 \text{ dB}$  corner points, at 145 kHz and 19.9 MHz marked  $\times$ , and (b) impulse response in the time domain.

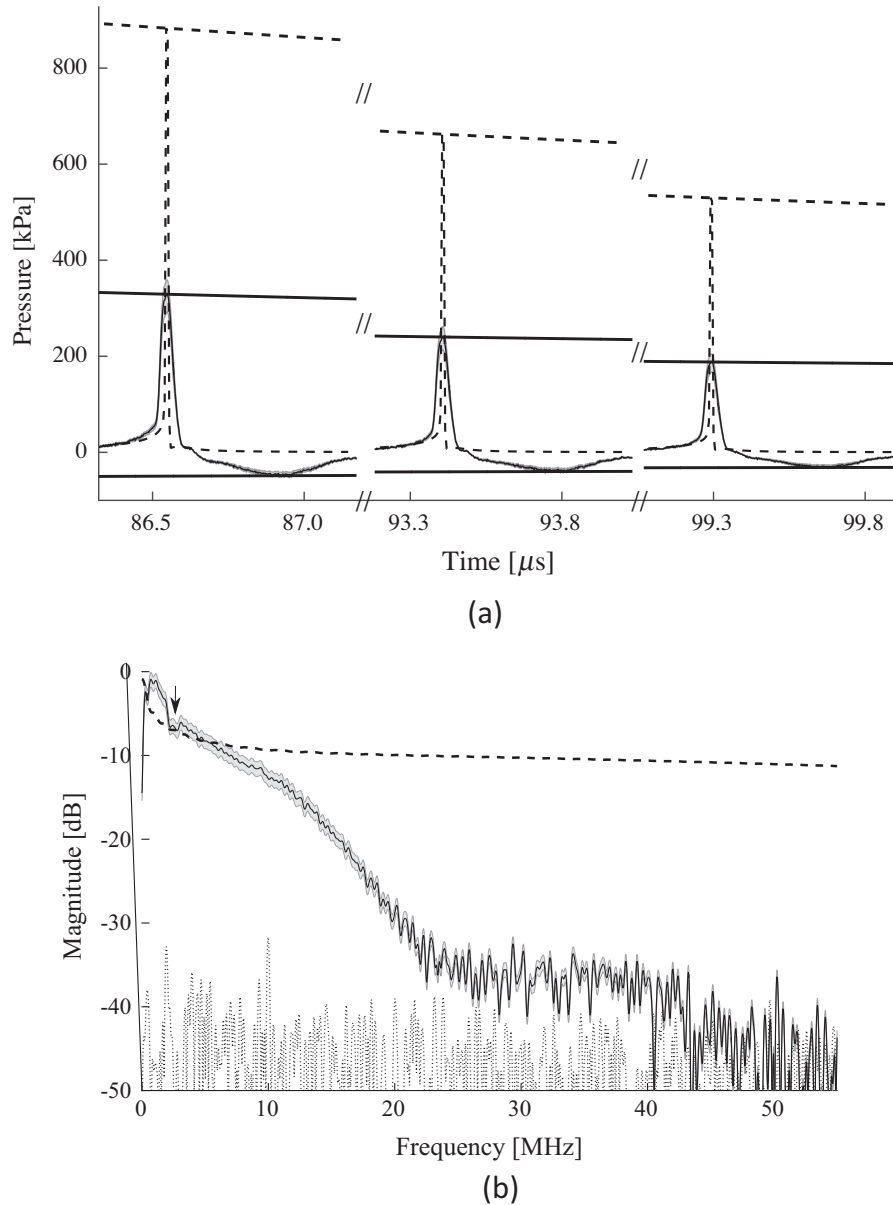


**Fig. 5.** (a) Single-frequency calibrated hydrophone signal (black with grey shaded uncertainty), with the calibration value at 10 MHz, for BCSWs measured at propagation distances of 30, 40 and 50 mm, and the simulated shock wave profile prediction (black dash). (b) Frequency spectra of the single-frequency calibrated signal (black with grey envelope) and simulated shock (black dash) at  $r = 30$  mm, normalised to the experimental data. Also shown (grey dot) is the noise floor, sampled from the hydrophone data between the Q-switch and the OBSW, Fig. 2(b).

#### 4. Deconvolution of hydrophone data

Deconvolution of the needle hydrophone data, [20] is performed in the frequency domain, according to Eq. (8)

$$P(f) = V(f)/M(f) \times H_{bpf}(f) \quad (8)$$

where  $P(f)$  is the deconvolved signal,  $V(f)$  the voltage signal,  $M(f)$  the complex sensitivity, and  $H_{bpf}(f)$  a bandpass filter, Fig. 4(a), implemented in the frequency domain and matching the calibration bandwidth of 125 kHz–20 MHz.

Applying an inverse Fourier transform, the deconvolved signal is obtained in the time domain. Magnitude-only deconvolution follows an equivalent process, assuming the phase,  $\varphi = 0^\circ$ , for all frequencies. Uncertainties in the frequency domain are computed in accordance with [32].

#### 5. Results

For the results reported below, BCSWs are measured by the needle hydrophone, with the tip located at three propagation distances,  $r = 30, 40$  and  $50 (\pm 0.5)$  mm from the laser focus and the LIBs that form. A BCSW dataset was collected from comparable LIBs, in terms of  $R_{max}$ , single-fronted shock wave generation and spherical rebound phase, verified via high-speed imaging, as discussed previously. Accordingly, the BCSWs presented may be considered as representative of the propagation of a single shock wave, such that propagation effects may also be assessed. Close to the bubble location, it may be expected that the BCSW speed is supersonic, during which the PPA decays as  $\sim r^{-2}$  [5]. At the measurement distances of 30–50 mm, however, it is expected that the pressure amplitude decays as  $\sim r^{-1}$  [5,10]. As such, we include broken  $r^{-1}$  envelopes across the peak pressures in each shock

wave representation, including for the simulated data, according to Eq. (7).

### 5.1. Single-frequency calibration

The shock profiles of Fig. 5(a), solid black line, are single-frequency calibrated BCSWs, converted from voltage to pressure using the magnitude sensitivity at 10.0 MHz, which is  $810.0 \pm 8.1$  mV/MPa. This frequency was selected as representative of how bubble shock wave literature is often reported, and also as it is within the flat bandwidth of the needle hydrophone, Fig. 1(b), thereby making it a suitable choice for demonstrating the assumption and implications of a flat frequency response. The time waveform shape of the profile is otherwise identical to the voltage signal detected by the hydrophone.

The black-dash profiles of Fig. 5(a) are the BCSWs predicted by the acoustic emissions computed by Eq. (7), from the solution of the Gilmore equation, with notable differences to those measured. In particular, the pressure amplitudes of the model profiles are

around 2.5 times greater than the measured values, and the FWHM less than 25% of those measured, Table 1. Furthermore, the experimental profiles all exhibit an apparent negative phase, lasting  $\sim 0.5$   $\mu$ s and propagation independent, trailing the compressive phase of the shock wave. The amplitude of the apparent negative phase also follows the  $r^{-1}$  decay, exhibited by its positive pressure counterpart (broken envelopes, Fig. 5(a)).

Fig. 5(b) are the frequency spectra of the experimental and simulated BCSW, at  $r = 30$  mm. The shape of the spectrum, convolved with the hydrophone response, is best considered relative to the calibration data of Fig. 1(b). The steeper fall-off in the magnitude of frequency components  $>12$  MHz corresponds to the marked decrease in magnitude sensitivity exhibited  $>12$  MHz. Moreover, the dip (arrowed, Fig. 5(b)) in the magnitude of the experimental BCSW spectrum, from 2 to 3 MHz, is likely due to the structure in the end-of-cable magnitude calibration data over the same frequency range, Fig. 1(b). The unfiltered simulated shock wave computed with a 100 MHz bandwidth, and a spectrum indicating greater magnitude at higher frequencies compared to the mea-

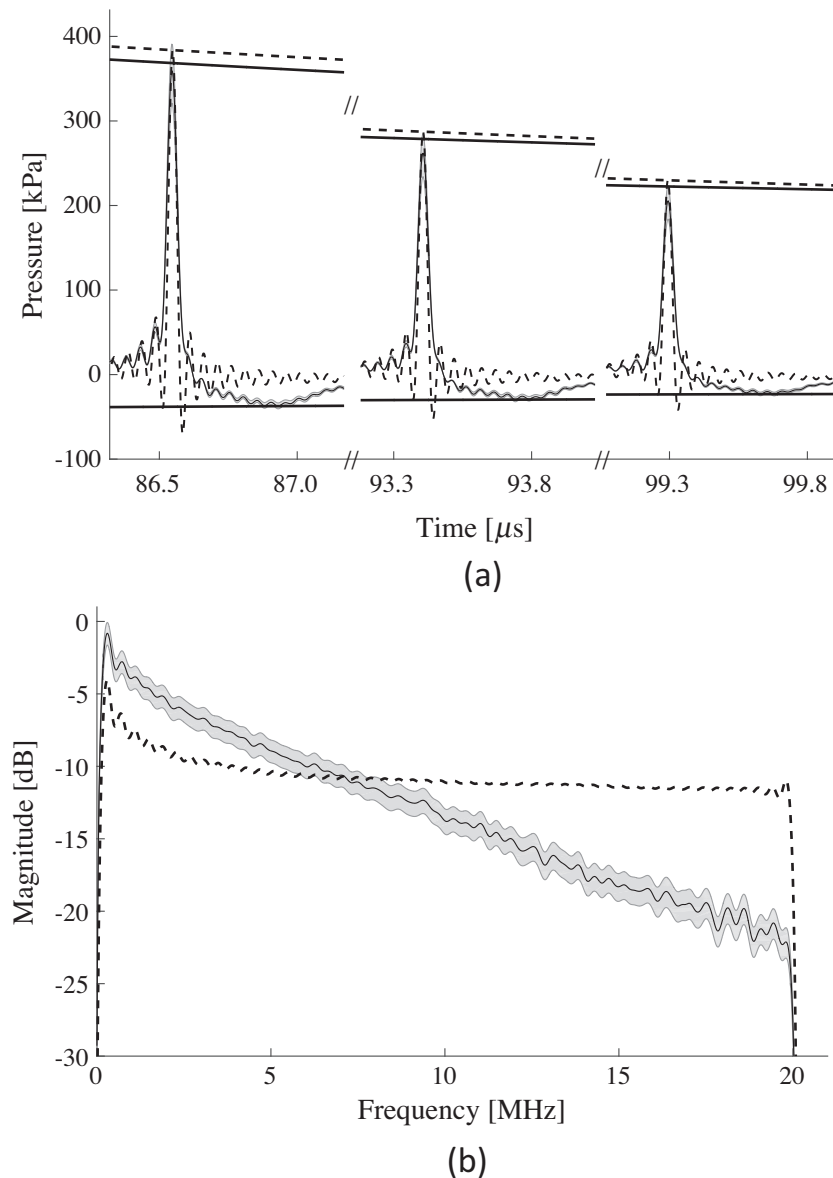


**Fig. 6.** (a) Magnitude-only deconvolved hydrophone signal (black with grey shaded uncertainty), at propagation distances of 30, 40 and 50 mm, and filtered simulated shock wave profile (black dash). (b) Frequency spectra of the magnitude-only deconvolved signal (black with grey envelope) and simulated shock (black dash) at  $r = 30$  mm, normalised to the experimental data.

sured shock wave, predictably has a narrower FWHM in the time domain, Fig. 5(a).

By sampling the hydrophone output between the Q-switch and the OBSW, a noise floor for the hydrophone system is identified at  $-45$  dB, grey dot, Fig. 5(b). The spectrum of the detected shock wave falls to this value at  $\sim 45$  MHz, indicating the needle hydrophone has sensitivity over a bandwidth beyond the calibration range of  $125$  kHz– $20$  MHz, as expected from the assessment of the rise time of the device, Section 2. However, it should be noted that if the bandwidth of the calibration is extended beyond where the measured signal is above the noise floor ( $\sim 45$  MHz for Fig. 5(b)), then deconvolution would only amplify high frequency noise [21]. Approximately 98% of the power above the noise floor, in the voltage trace of the measured shock wave is within the calibrated range, which gives some confidence that the calibration bandwidth for the needle hydrophone is sufficient for deconvolution of BCSW, and an assessment of the shock wave characteristics. For subsequent comparisons between simulated and experimental measurements, we therefore apply  $H_{bpf}(f)$ , Fig. 4, to the simulated shock wave profiles and spectra, such that the bandwidths considered are equivalent. The spectra are therefore subsequently presented from 0 to 20 MHz.

### 5.2. Magnitude-only deconvolution

The experimental BCSW profiles of Fig. 6(a) are magnitude-only deconvolved according to Eq. (8), with  $\varphi = 0$  for  $M(f)$ . Direct comparison with the single-frequency calibrated data, Table 1, indicates that magnitude-only deconvolution, Table 2, has increased the peak positive pressure amplitudes by  $\sim 9\%$ . At rapid pressure variations within the BCSW profile, a rippling artefact is introduced due the bandpass filter  $H_{bpf}(f)$  suppressing frequency content outside the calibration bandwidth, as a manifestation of the Gibbs' effect, also apparent in Fig. 4. This rippling prevents meaningful measurement of the rise time (RT) of the experimentally measured shock waves. An equivalent filter is applied to the simulated shock wave profiles of Fig. 6(a), black-dash, for comparison to magnitude-only deconvolved hydrophone data, which also generates the Gibbs' effect. The filtering also reduces the pressure amplitude of the simulated shock wave profiles.

Note, however, that the apparent negative phase has been preserved through the magnitude-only deconvolution, in accordance with assuming  $\varphi = 0^\circ$  for all frequencies, Fig. 6(a).

Fig. 6(b) are the spectra of the shocks at 30 mm with the effect of  $H_{bpf}(f)$  clearly evident. As expected for a shock wave generally, the experimental spectrum now decays with a better approximation to linearity in the dB scale, at increasing frequency. For all frequencies with a sensitivity lower than that at 10 MHz, Fig. 1(b), the magnitude at the respective frequency components are increased according to Eq. (8), most notably  $>12$  MHz. Also, the dip (arrowed Fig. 5(a)) in the spectrum of the single-frequency calibration BCSW has been removed by magnitude-only deconvolution. Comparison to Fig. 5(b) indicates that the pressure amplitudes for the different frequency components are therefore better estimated in the frequency domain, compared to the single frequency calibration, as the whole bandwidth of calibration is utilised correcting for the non-flat magnitude response.

The Gibbs' effect is manifested in the spectrum of the simulated shock wave, Fig. 6(b), at the limits of the bandpass filter, and is also apparent toward the low frequency limit of the filter in the experimental spectrum.

### 5.3. Full waveform deconvolution

Fig. 7 depicts the full waveform deconvolution of the BCSW hydrophone data, incorporating the phase calibration data. It is observed that the apparent negative phases of the experimental BCSW profiles have been removed when the phase response to the hydrophone system is corrected for.

The peak positive pressure amplitude of the full waveform deconvolved profile is  $\sim 3\%$  higher at each propagation distance, than those of the magnitude-only deconvolved profiles. The peak pressure amplitudes of the filtered simulated profiles are now within the calibration error provided by NPL, of the full waveform deconvolved BCSW amplitudes, in the time domain.

The frequency spectrum of the full waveform deconvolution is equivalent to that of the magnitude-only deconvolution, Fig. 6(b), as the magnitude in the frequency domain does not depend on the phase.

The FWHM for the experimental profiles, Table 3, are  $\sim 30\%$  longer than those of the filtered simulated profiles. This is due to the filtered simulated profiles having higher magnitude than the experimental profiles from  $\sim 10$  MHz, and lower magnitude for frequencies below, Fig. 6(b).

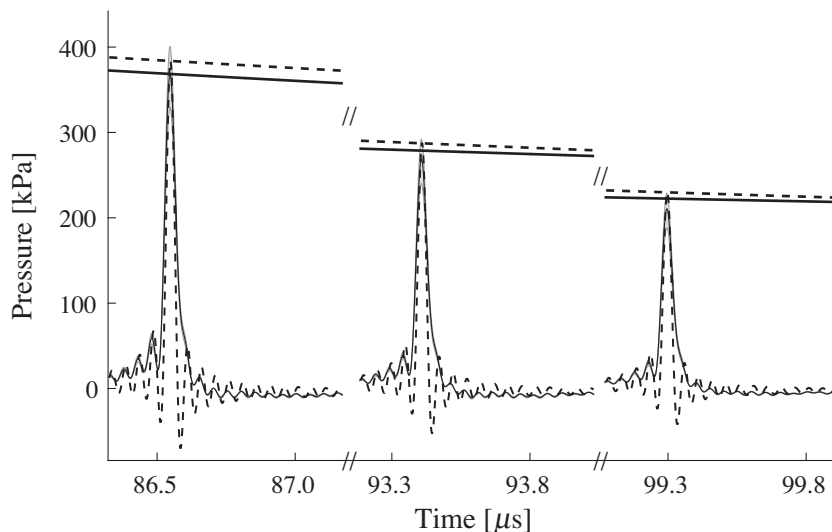


Fig. 7. Full waveform deconvolved hydrophone signal (black with grey shaded uncertainty), at propagation distances of 30, 40 and 50 mm, and filtered simulated shock wave profile (black dash).

**Table 1**

Shock wave properties from Fig. 5 (a), including rise time (RT), full width half maximum (FWHM) and peak positive pressure amplitude (PPA), for single-frequency calibration and simulated shock wave profile, at each of the propagation distances.

Prop distance (mm)	Single frequency calibration			Simulated shock profile		
	RT (ns)	FWHM (ns)	PPA (kPa)	RT (ns)	FWHM (ns)	PPA (kPa)
30	71	46	329 ± 36	5	10	883
40	53	47	240 ± 26	5	10	662
50	57	46	188 ± 21	5	10	529

**Table 2**

Shock wave properties from Fig. 6(a), including full width half maximum (FWHM) and peak positive pressure amplitude (PPA), for magnitude-only and filtered simulated shock wave profile, at each of the propagation distances.

Prop distance (mm)	Magnitude-only deconvolution		Simulated shock profile	
	FWHM (ns)	PPA (kPa)	FWHM (ns)	PPA (kPa)
30	44	359 ± 38	31	383
40	44	261 ± 27	31	287
50	45	205 ± 21	31	230

**Table 3**

Shock wave properties from Fig. 7(a), including full width half maximum (FWHM) and peak positive pressure amplitude (PPA), for full waveform deconvolved and filtered simulated shock wave profile, at each of the propagation distances.

Prop distance (mm)	Full waveform deconvolution		Simulated shock profile	
	FWHM (ns)	PPA (kPa)	FWHM (ns)	PPA (kPa)
30	45	368 ± 38	31	383
40	46	268 ± 28	31	287
50	47	210 ± 23	31	230

## 6. Discussion

We have recently reported the role of periodic shock waves in the emissions generated by a cloud of acoustic cavitation bubbles, and the contribution to the subharmonic ( $f_0/n$ , where  $f_0$  frequency of the acoustic driving) signal, and the higher-order subharmonics ( $mf_0/n$ ), in particular [16]. This motivated the current work on how to treat detected bubble collapse shock waves, such that their contribution to the emission may be quantitatively analysed, in particular for hydrophones with a non-flat frequency response.

Generally, studies that seek to develop cavitation applications will present the spectrum of the emissions collected, and typically link a feature within the spectrum to the cavitation-mediated effect under investigation. The magnitude of that feature is often taken as an indicator of the level of cavitation that occurred, commonly as a result of and increased pressure amplitude of the acoustic driving. The subharmonic, or higher-order subharmonics, are often used, as these signals have long been considered exclusive to stable or inertial acoustic cavitation activity [17]. The results reported above confirm that magnitude-only deconvolution has an influence on the spectrum of a single BCSW for a hydrophone with non-flat magnitude response. To perform quantitative analysis on the subharmonic and higher-order subharmonic peaks, from cavitation spectra with shock wave content, it is therefore necessary to use a detecting device that is calibrated for magnitude response, over an appropriate bandwidth with respect to spectral features that are being monitored. This includes bespoke passive cavitation devices, particularly broadband PVdF-based detectors, where shock wave detection may be expected to constitute a significant proportion of the signal collected. If the purpose of the measurement is to reconstruct the shock wave in the time-domain, for the whole bandwidth of the shock wave with a precise estimate of PPA, then a spot-poled membrane [21] or fibre-optic

hydrophone [33] would be recommended, over a 1 mm PVdF needle-type hydrophone with a comparatively limited bandwidth. Space limitations within a given experimental set-up, and signal-to-noise requirements for the detection of low PPA shock waves, respectively, may preclude the use of such devices. In any case, magnitude-only deconvolution would go some way to facilitating direct comparison of the cavitation spectra presented during different studies [34,35] from different research groups provided the same bandwidth is compared, which is an issue in current literature. Moreover, quantitative analysis of inertial cavitation emissions that contains shock wave components, in the time domain, can only be meaningfully implemented with full waveform deconvolution for detectors with a non-flat frequency response, with magnitude and phase calibration data.

This extends to techniques being developed for real time and spatial monitoring of cavitation activity, such as passive acoustic mapping [36,37] during the application of therapeutic ultrasound in the MHz regime. Appropriate calibration of the array elements used would allow more meaningful interpretation of cavitation activity.

All bubble collapse shock wave generation models in the literature predict purely compressive shock wave profiles [5,8,13,31], also confirmed experimentally using optical techniques [38]. BCSW propagation, however, is not so well studied and many reports present measurements, taken with a range of detecting devices, which include an apparent trailing negative phase. Shock waves generally, such as those resulting from a detonation [39] or used for lithotripsy [15], are known to develop a tensile phase following the initial impulsive compression, attributed at least in part to medium response to the propagating compression. The results presented in this paper indicate that this is not the case, at least for BCSWs from a collapsing LIB formed in water, and that the reported apparent negative phases are detector convolution arte-

facts, such as those in Figs. 5(a) and 6(a). Such convolution artefacts become more noticeable for detectors with a non-flat frequency response.

It is observed in Fig. 5(a) and Table 1 that the simulated profiles have FWHM  $\sim 25\%$  of those measured with the needle hydrophone. The simulated profiles were computed with a bandwidth of 100 MHz, in addition it is seen in Fig. 5(b) that all frequency content  $>6$  MHz is overestimated, and so it would be expected to have FWHM shorter than those measured. However, both types of deconvolution, which are compared to filtered simulated profiles, also exhibit FWHM  $\sim 70\%$  of the measured values, Tables 2 and 3. A spherically propagating shock wave incident to a detector with a finite active area will introduce a geometrical spreading effect to the measurement. Consideration of the experimental setup described, and assuming an impulse shock wave, propagating at the speed of sound at the distances measurements were taken, indicates a spreading of  $\sim 3$  ns. Of course, the physical shock wave will have some finite width, and so the effect will be larger than for an impulse. One consequence of this effect will be that the measurements of both RT and FWHM will be overestimated.

In Fig. 6(b) it is seen that the frequency content  $>10$  MHz is overestimated by the simulation, although this difference should reduce if experimental attenuation is taken into account. For a continuous wave at 10 MHz and 20 MHz it is expected to be attenuated 0.07 dB and 0.14 dB after 30 mm of propagation, respectively, although this effect may be expected to be stronger during early supersonic propagation of the BCSW from the bubble. This would shift the shape of the simulated BCSW spectrum closer to that of the measured one, particularly for frequencies above 10 MHz.

The spectrum of the magnitude-only, and consequently the full waveform deconvolved BCSW hydrophone data, Fig. 6(b), indicate that the intensity decreases linearly with increasing frequency. Indeed, it is clear that the majority of the BCSW intensity is contained in the lower frequency region of the spectrum, with the magnitude falling below  $-10$  dB at 5 MHz, Fig. 6(b). This suggests that designing detectors for maximum sensitivity at lower frequencies should be considered, if detecting periodic shock waves and subharmonic signals from acoustic cavitation, is desired.

Possible improvements to this work include a more rigorous simulation of the bubble collapse, accounting for factors such as gas content, heat and mass transfer in the bubble oscillation model would influence the collapse dynamic, and subsequently the predicted shock wave. Moreover there are advanced shock wave generation models [6,14,31,40], which account for compressibility of the medium through which the shock wave is propagating, for example. Implementing a more refined BCSW simulation may deliver better matching spectra to those measured experimentally with a wider calibration bandwidth. However, for the purposes of investigating the effects of deconvolution on cavitation bubble shock waves, and providing insight into how they may be treated with the appropriate hydrophone calibration, the results presented suggest the approaches adopted are adequate. In this work we report end-of-cable sensitivity, where the complex sensitivity is a convolution of the needle and the pre-amplifier associated with the system. Obtaining the complex sensitivity to the pre-amplifier would allow for further deconvolution of the end-of-cable sensitivity such that the non-flat structure of the frequency response could be better understood.

## 7. Conclusions

Single-frequency calibration of experimentally detected BCSWs delivers profiles with notable differences to simulation predictions, generated via a bubble collapse and simple acoustic emission model. Magnitude-only deconvolution, in comparison to appropri-

ately filtered simulation profiles, improves the PPA estimate of the experimental measurement, but the waveform in the time domain retains phase distortion. Full waveform deconvolution provides the best match between the experimentally measured and filtered simulation data, removing the non-flat detector response within the calibration bandwidth; most notably the apparent negative phase.

## Acknowledgements

The research leading to these results has received funding from the European Research Council under the European Union's Seventh Framework Programme (FP/2007 – 2013)/ERC Grant Agreement no. 336189 (TheraCav). The authors acknowledge Graeme Casey and Miriam Jiménez García for technical assistance, Prof. Sandy Cochran and Dr. Holly Lay for constructive discussions.

## Appendix A. Supplementary data

Supplementary data associated with this article can be found, in the online version, at <http://dx.doi.org/10.1016/j.ultras.2016.09.007>.

## References

- [1] D.J. Flannigan, K.S. Suslick, Plasma formation and temperature measurement during single-bubble cavitation, *Nature* 434 (2005) 52–55.
- [2] M.W. Miller, D.L. Miller, A.A. Brayman, A review of in vitro bioeffects of inertial ultrasonic cavitation from a mechanistic perspective, *Ultrasound Med. Biol.* 22 (1996) 1131–1154.
- [3] L.H. Thompson, L.K. Doraiswamy, *Sonochemistry: science and engineering*, Ind. Eng. Chem. Res. 38 (1999) 1215–1249.
- [4] B.P. Barber, S.J. Putterman, Observation of synchronous picosecond sonoluminescence, *Nature* 352 (1991) 318–320.
- [5] A. Vogel, S. Busch, U. Parlitz, Shock wave emission and cavitation bubble generation by picosecond and nanosecond optical breakdown in water, *J. Acoust. Soc. Am.* 100 (1996) 148–165.
- [6] E.A. Brujan, A. Vogel, Stress wave emission and cavitation bubble dynamics by nanosecond optical breakdown in a tissue phantom, *J. Fluid Mech.* 558 (2006) 281–308.
- [7] E.A. Brujan, Shock wave emission from laser induced cavitation bubbles in polymer solutions, *Ultrasonics* 48 (2008) 423–426.
- [8] S.W. Krang, Y.P. Lee, K.Y. Kim, H.Y. Kwak, Implosion mechanism for a sonoluminescing gas bubble, *J. Korean Phys. Soc.* 43 (2003) 135–144.
- [9] T. Asase, Y. Watanabe, Observation of shock wave propagation by a sonoluminescing bubble, *Jap. J. Appl. Phys.* 43 (2004) 403–404.
- [10] E.A. Brujan, T. Ikeda, Y. Matsumoto, Shock wave emission from a cloud of bubbles, *Soft Matter* 8 (2012) 5777–5783.
- [11] Y. Brelet, A. Jarnac, J. Carbonnel, Y.B. Andre, A. Mysyrowicz, A. Houard, Underwater acoustic signals induced by intense ultrashort laser pulse, *JASA-EL* 137 (2015) EL288–EL292.
- [12] K.R. Weninger, B.P. Barber, S.J. Putterman, Pulsed Mie scattering measurements of the collapse of a sonoluminescing bubble, *Phys. Rev. Lett.* 78 (1997) 1799–1802.
- [13] C.E. Brennen, Cavitation in medicine, *Interface Focus* 5 (2015) 2010022.
- [14] S.L. Ceccio, C.E. Brennen, Observations of the dynamics and acoustics of travelling bubble cavitation, *J. Fluid Mech.* 233 (1991) 633–660.
- [15] Y. Zhou, Reduction of bubble cavitation by modifying the diffraction wave from a lithotripter aperture, *J. Endourol.* 26 (2012) 1075–1084.
- [16] K. Johnston, C. Tapia-Siles, B. Gerold, M. Postema, S. Cochran, A. Cuschieri, P. Prentice, Periodic shock-emission from acoustically driven cavitation clouds: a source of the subharmonic signal, *Ultrasonics* 54 (2014) 2151–2158.
- [17] T.G. Leighton, *The Acoustic Bubble*, Academic Press, London, 1994, pp. 414.
- [18] G.R. Harris, R.C. Preston, A.S. DeReggi, The impact of piezoelectric PVDF on medical ultrasound exposure measurements, standards, and regulations, *IEEE UFFC* 47 (2000) 1321–1335.
- [19] A. Shaw, M. Hodnett, Calibration and measurement issues for therapeutic ultrasound, *Ultrasonics* 48 (2008) 234–252.
- [20] A. Hurrell, Voltage to pressure conversion: are you getting 'phased' by the problem?, *J Phys: Conf. Ser.* 1 (2004) 57–62.
- [21] V. Wilkens, S. Sonntag, O. Georg, Robust spot-poled membrane hydrophones for measurement of large amplitude pressure waveforms generated by high intensity ultrasonic transducers, *J. Acoust. Soc. Am.* 139 (2016) 1319–1332.
- [22] D. Kröniger, K. Köhler, T. Kurz, W. Lauterborn, Particle tracking velocimetry of the flow field around a collapsing cavitation bubble, *Exp. Fluids* 48 (2010) 395–408.
- [23] J.B. Keller, Bubble oscillations of large amplitude, *J. Acoust. Soc. Am.* 68 (1980) 628–633.

- [24] C. Herring, Theory of the pulsation of the gas bubble produced by an underwater explosion, U.S Office of Scientific Research and Development, Tech Rep., 1941.
- [25] F.R. Gilmore, The growth or collapse of a spherical bubble in a viscous compressible liquid, *Calif. Inst. Tech. Eng. Rep.* 26 (1952) 1–40.
- [26] W. Kreider, L.A. Crum, M.R. Bailey, O.A. Sapozhnikov, A reduced-order, single-bubble cavitation model with applications to therapeutic ultrasound, *J. Acoust. Soc. Am.* 130 (2011) 3511–3530.
- [27] H.G. Flynn, Cavitation dynamics. I. A mathematical formulation, *J. Acoust. Soc. Am.* 57 (1975) 1379–1396.
- [28] A. Prosperetti, A. Lezzi, Bubble dynamics in a compressible liquid. Part 1. First-order theory, *J. Fluid Mech.* 168 (1986) 457–478.
- [29] J.R. Macdonald, Some simple isothermal equations of state, *Rev. Mod. Phys.* 38 (1966) 666–679.
- [30] H. Lin, B.D. Storey, A.J. Szeri, Inertially driven inhomogeneities in violently collapsing bubble: the validity of the Rayleigh-Plesset equation, *J. Fluid Mech.* 452 (2002) 145–162.
- [31] M. Koch, C. Reuter, F. Köhler, K. Mettin, W. Lauterborn, Numerical modeling of laser generated cavitation bubbles with the finite volume and volume of fluid method, using OpenFOAM, *Comput. Fluids* 126 (2016) 71–90.
- [32] S. Eichstädt, V. Wilkens, GUM2DFT – a software tool for uncertainty evaluation of transient signals in the frequency domain, *Meas. Sci. Technol.* 27 (2016) 055001.
- [33] S. Umchid, R. Gopinath, K. Srinivasan, P.A. Lewin, A.S. Daryoush, L. Bansal, M. El-Sherif, Development of calibration techniques for ultrasonic hydrophone probes in the frequency range from 1 to 100 MHz, *Ultrasonics* 49 (2009) 306–311.
- [34] D.M. Hallow, A.D. Mahajan, T.E. McCutchen, M.R. Prausnitz, Measurement and correlation of acoustic cavitation with cellular bioeffects, *Ultrasound Med. Biol.* 32 (2006) 1111–1122.
- [35] M. Schoellhammer, A. Schroeder, R. Maa, G.Y. Lauwers, A. Swiston, M. Zervas, R. Barman, A.M. DiCiccio, W.R. Brugge, D.G. Anderson, D. Blankschtein, R. Langer, G. Traverso, Ultrasound-mediated gastrointestinal drug delivery, *Sci. Transl. Med.* 7 (2015) 310ra168.
- [36] M. Gyongy, C.C. Coussios, Passive acoustic mapping of inertial cavitation during HIFU exposure, *IEEE Trans. Biomed. Eng.* 57 (2010) 48–56.
- [37] R.M. Jones, M.A. O'Reilly, K. Hynynen, Transcranial passive acoustic mapping with hemispherical sparse arrays using CT-based skull specific aberration corrections: a simulation study, *Phys. Med. Biol.* 58 (2013) 4981–5005.
- [38] C.F. Delale (Ed.), *Bubble Dynamics & Shock Waves, SHOCKWAVES 8*, Springer-Verlag, Berlin, Heidelberg, 2013, pp. 67–103.
- [39] S.E. Rigby, A. Tyas, T. Bennet, S.D. Clarke, S.D. Fay, The negative phase of the blast load, *Int. J. Protective Struct.* 5 (2014) 1–20.
- [40] S.J. Shaw, P.D.M. Spelt, Shock emission from collapsing gas bubbles, *J. Fluid Mech.* 646 (2010) 363–373.